Available online at www.sciencedirect.com

SCIENCE DIRECT®

PERGAMON

International Journal of Multiphase Flow 29 (2003) 721–750

International Journal of Multiphase Flow

www.elsevier.com/locate/ijmulflow

Particle deposition from two-dimensional turbulent gas flows

S.A. Slater, A.D. Leeming, J.B. Young *

Hopkinson Laboratory, Cambridge University Engineering Department, Trumpington Street, Cambridge CB2 1PZ, UK

Received 25 April 2002; received in revised form 19 February 2003

Abstract

The paper is concerned with the prediction of the deposition rate of small particles from two-dimensional turbulent gas flows onto solid boundaries using a fully-Eulerian two-fluid approach. Density-weighted averaging is used to derive the ensemble-averaged particle equations which are closed with simple models for the particle turbulence correlations. A possible inconsistency in the modelling is discussed. A special method of handling the equations provides much clearer insight into the physical processes governing deposition. The solution procedure uses a formulation which can automatically capture particle-free regions and can predict surface deposition rates which may vary by several orders of magnitude. This is illustrated via calculations of deposition from turbulent channel-flow which also allow prediction of the inlet region where the particle flow is not fully-developed. Deposition from turbulent boundary layers is also considered and calculations showing the interaction between velocity slip (caused by streamline curvature), viscous drag, diffusion and turbophoresis are presented. The ability to handle complex geometries is illustrated by a calculation of deposition in a gas turbine cascade. This also provides an illustration of how inertial and diffusional deposition mechanisms work in concert and how the sum of the contributions considered separately does not represent the total deposition rate. Some preliminary calculations and experimental data on the effect of thermophoresis in non-isothermal flows are also presented.

1. Introduction

The widespread occurrence of dispersed gas–particle flows in natural and industrial processes has provided the impetus for their extensive study, resulting in numerous research publications. Most of these deal with particle motion in free turbulent flows where solid boundaries exert no influence. Far fewer publications have been devoted to the prediction of particle deposition onto

* Corresponding author. Tel.: +44-1223-330263.
E-mail address: jby@eng.cam.ac.uk (J.B. Young).

0301-9322/03/$ - see front matter
doi:10.1016/S0301-9322(03)00037-5

boundary surfaces and virtually all of this work is concerned with deposition in fully-developed pipe-flow. This paper extends the theory and computational capability to the prediction of deposition from two-dimensional flows where streamline curvature may influence particle transport both in the free-stream and in the turbulent boundary layers.

Many publications describe calculations of the inertial deposition of particles from 2D flows where the influence of turbulence is unimportant. Most adopt a Lagrangian approach whereby the particle equations are integrated along particle pathlines. In such deterministic flows, comparatively few pathline calculations give a good representation of the particle velocity field. The particle density field can also be determined accurately and efficiently if the so-called *full-Lagrangian* approach is used (Healy and Young, 2001).

Difficulties arise when the particles respond to the fluid turbulence because Lagrangian methods must now include a stochastic element. In the original formulation of Gosman and Ioannides (1983), the flowfield was obtained by the random sampling of a crude turbulence model at each time-step. A deposition calculation using a similar method has been reported by Kallio and Reeks (1989) but problems arise in dealing with very small particles when Brownian diffusion is important. Improved representations of the turbulence can be obtained by using *Large Eddy Simulations* (Wang et al., 1998) or *Direct Numerical Simulations* (Squires and Eaton, 1991), but the computation time is much greater, particularly for DNS. These techniques are useful as research tools but are not suitable for engineering calculations.

When turbulence is important, the two-fluid Eulerian approach is computationally more efficient and is the method adopted for the present work. The difficulty here is to provide closure models for the averaged particle equations of motion. In recent years much progress has been made by Derevich and Zaichik (1988), Derevich (1999), Reeks (1991, 1992), Hyland and Reeks (1997), Simonin et al. (1993) and others. A two-fluid model, designed specifically with deposition in mind, has also been reported by Young and Leeming (1997), hereafter referred to as YL97. Their method of handling the equations emphasises the differing rôles played by diffusion (particle fluxes driven by density gradients) and turbophoresis (fluxes driven by fluctuating velocity gradients). Turbophoresis was first mentioned by Caporaloni et al. (1975) and Reeks (1983), and is now known to be the main mechanism for transporting particles with substantial inertia in turbulent wall layers.

Even if suitable closure models can be found, the Eulerian approach is not without its difficulties if the flowfield boundaries are geometrically complicated. Indeed, even in the absence of turbulence, numerical problems arise involving the accurate representation of particle density discontinuities, the capture of particle-free zones, and the physically correct treatment of solid boundaries. It is only recently that these issues have begun to be addressed in the literature (Slater and Young, 2001). This is probably because most deterministic particle flows in difficult geometries are still computed using a Lagrangian approach and most Eulerian calculations of turbulent particle flows have been confined to simple situations.

In this paper, the fully-Eulerian computational method of Slater and Young (2001) is extended to include the effects of turbulence on deposition. The theoretical approach is similar to that described in YL97 for the special case of deposition from turbulent pipe-flow, the main difference being that particle-density-weighted rather than non-density-weighted averaging of the particle equations of motion is used in the present work. Density-weighted averaging has the advantage that fewer turbulence correlations are generated. This does not necessarily imply, of course, that

the modelling is more accurate and, indeed, an apparent inconsistency in conventional particle turbulence modelling is noted and discussed.

The form of the paper is as follows. In Section 2, the averaged particle equations of motion and the turbulence closure models are presented. In Section 3, the 2D numerical solution procedure is briefly described. In Section 4 calculations of deposition from turbulent channel-flow are presented to provide validation for the method. Section 5 then describes how free-stream conditions can modify turbulent transport in boundary layers. Section 6 describes the deposition of small particles onto gas turbine blades and is included to highlight an important application and to show the potential for extension to other engineering problems.

2. Theory

2.1. Particle conservation equations

Consider the flow of small spherical mono-dispersed particles suspended in a carrier gas. The analysis is restricted to dilute suspensions meaning that the fluid motion is unaffected by the presence of the particles and that particle–particle collisions can be neglected. The conditions under which these assumptions are valid have been stated many times. A particularly illuminating account can be found in Tsirkunov (2001).

Using Cartesian tensor notation with the repeated suffix summation convention, the conservation equations for particle mass and momentum can be written,

$$\frac{\partial \rho_{\mathrm{p}}}{\partial t} + \frac{\partial (\rho_{\mathrm{p}} v_k)}{\partial x_k} = 0 \tag{1a}$$

$$\frac{\partial (\rho_{\mathrm{p}} v_i)}{\partial t} + \frac{\partial (\rho_{\mathrm{p}} v_i v_k)}{\partial x_k} = \rho_{\mathrm{p}} F_i = \rho_{\mathrm{p}} (F_{\mathrm{D},i} + F_{\mathrm{L},i} + F_{\mathrm{T},i} + F_{\mathrm{B},i}) \tag{1b}$$

where ρ_{p} is the particle density (mass of particles per unit volume), v_i is the i-component of the particle velocity and F_i is the i-component of the force per unit mass acting on the particles. Adopting the usual dusty gas approximations and neglecting gravity, the most important forces are those associated with steady-state viscous drag, shear-flow lift, thermophoresis and Brownian motion. These are denoted by subscripts D, L, T and B respectively.

The steady-state drag force per unit particle mass is written,

$$F_{\mathrm{D},i} = \frac{(u_i - v_i)}{\tau_{\mathrm{p}}} \tag{2a}$$

where u_i is the i-component of the gas velocity and τ_{p} is the local particle inertial relaxation time. For Stokes drag, τ_{p} is independent of the slip velocity and is given by $\tau_{\mathrm{p}} = d_{\mathrm{p}}^2 \rho_{\mathrm{mat}} / 18 \mu_{\mathrm{g}}$ where d_{p} is the particle diameter, ρ_{mat} is the particle material density and μ_{g} is the gas dynamic viscosity. If the slip Reynolds number exceeds about unity, the expression for τ_{p} should be modified by, for example, the well-known empirical expressions of Morsi and Alexander (1972). Unfortunately, the linear relationship between $F_{\mathrm{D},i}$ and $(u_i - v_i)$ is then compromised.

An expression for the shear-flow lift force on a particle was first derived by Saffman (1965). An instructive way of writing Saffman's expression which brings out the dependence on τ_p is,

$$F_{L,i} = K_L \sum_{\substack{k=1 \\ k\neq i}}^{3} \left[\left(\frac{\rho_g}{\rho_{mat}} \tau_p \frac{\partial u_k}{\partial x_i} \right)^{1/2} \frac{(u_k - v_k)}{\tau_p} \right] \tag{2b}$$

where $F_{L,i}$ is the force per unit particle mass in the i-direction, ρ_g is the carrier gas density and the summation on k does *not* include the i-component. In Saffman's original theory, the constant $K_L = 0.725$ but a number of modifications have appeared in the literature since his original paper and are discussed by Wang et al. (1997). These can be included if desired.

The thermophoretic force per unit particle mass can be written,

$$F_{T,i} = \frac{K_T \nu_g}{\tau_p} \frac{\partial(\ln T_g)}{\partial x_i} \tag{2c}$$

where $\nu_g = \mu_g/\rho_g$ and T_g is the gas temperature. K_T is a coefficient which depends on the ratio of the gas and particle thermal conductivities. K_T is usually given by the empirical expression of Talbot et al. (1980) which is not reproduced here. Eq. (2c) has also been written in a form to bring out the dependence on τ_p.

The Brownian force per unit particle mass is given by,

$$F_{B,i} = -\frac{1}{\rho_p} \frac{\partial p_p}{\partial x_i} = -\frac{kT_g}{m_p} \frac{\partial(\ln \rho_p)}{\partial x_i} = -\frac{D_B}{\tau_p} \frac{\partial(\ln \rho_p)}{\partial x_i} \tag{2d}$$

where p_p is the particle partial pressure due to random thermal motion, k is Boltzmann's constant, m_p is the mass of a particle and D_B is the Brownian diffusion coefficient, given by Einstein's equation $D_B = kT_g/\tau_p m_p$. The derivation of this equation and a good discussion on Brownian diffusion is given by Ramshaw (1979).

2.2. Averaged particle equations for turbulent flow

For turbulent flow, the instantaneous particle conservation equations must be averaged. Particle density-weighted averaging was used by Simonin et al. (1993), Derevich and Zaichik (1988) and Hyland and Reeks (1997), but YL97 used non-density-weighted averaging. Density-weighted averaging is popular because fewer turbulence terms are generated but this does not necessarily mean that the turbulence modelling is more accurate.

Because of the algebraic advantages, density-weighted ensemble averaging is used here. Accordingly, ρ_p and the gas velocity u_i are decomposed into an ensemble-mean quantity (denoted by an overbar) and a fluctuating component (denoted by a single prime). Thus,

$$\rho_p = \bar{\rho}_p + \rho'_p \quad (\overline{\rho'_p} = 0)$$

$$u_i = \overline{U}_i + u'_i \quad (\overline{u'_i} = 0)$$

Other quantities are decomposed into a density-weighted ensemble-mean (denoted by a double overbar) and a fluctuating component (denoted by a double prime). Thus,

$$\rho_{\mathrm{p}} v_i = \rho_{\mathrm{p}} \overline{\overline{V_i}} + \rho_{\mathrm{p}} v_i'' \quad (\overline{\rho_{\mathrm{p}} v_i} = \bar{\rho}_{\mathrm{p}} \overline{\overline{V_i}},\ \ \overline{\rho_{\mathrm{p}} v_i''} = \bar{\rho}_{\mathrm{p}} \overline{\overline{v_i''}} = 0)$$

This notation is, the authors believe, much more easily readable and transparent than the ubiquitous, but awkward and often ambiguous, angled brackets $\langle \cdots \rangle$.

Applying this averaging process to Eqs. (1) gives the density-weighted, ensemble-averaged equations,

$$\frac{\partial \bar{\rho}_{\mathrm{p}}}{\partial t} + \frac{\partial (\bar{\rho}_{\mathrm{p}} \overline{\overline{V_k}})}{\partial x_k} = 0 \tag{3a}$$

$$\frac{\partial (\bar{\rho}_{\mathrm{p}} \overline{\overline{V_i}})}{\partial t} + \frac{\partial (\bar{\rho}_{\mathrm{p}} \overline{\overline{V_i V_k}})}{\partial x_k} + \frac{\partial (\bar{\rho}_{\mathrm{p}} \overline{\overline{v_i'' v_k''}})}{\partial x_k} = \overline{\rho_{\mathrm{p}} (F_{\mathrm{D},i} + F_{\mathrm{L},i} + F_{\mathrm{T},i} + F_{\mathrm{B},i})} \tag{3b}$$

The averaging of the force terms in Eq. (3b) requires comment. The drag force is normally dealt with by assuming τ_{p} to be a *local* constant evaluated at the local *mean* slip Reynolds number. This approximation has been validated to a certain extent by the calculations of Wang et al. (1998). Making this assumption gives,

$$\overline{\rho_{\mathrm{p}} F_{\mathrm{D},i}} = \bar{\rho}_{\mathrm{p}} \overline{\overline{F_{\mathrm{D},i}}} = \frac{\bar{\rho}_{\mathrm{p}} (\overline{U}_i - \overline{\overline{V_i}}) + \overline{\rho_{\mathrm{p}} u_i'}}{\tau_{\mathrm{p}}} = \frac{\bar{\rho}_{\mathrm{p}} (\overline{U}_i - \overline{\overline{V_i}} + \overline{\overline{u_i'}})}{\tau_{\mathrm{p}}} \tag{4a}$$

Averaging of the lift force term has not yet been addressed in the literature. Ignoring any correlation between fluctuating particle density and gas velocity results in,

$$\overline{\rho_{\mathrm{p}} F_{\mathrm{L},i}} = \bar{\rho}_{\mathrm{p}} \overline{\overline{F_{\mathrm{L},i}}} = K_{\mathrm{L}} \sum_{\substack{k=1 \\ k \neq i}}^{3} \left[\left(\frac{\rho_{\mathrm{g}}}{\rho_{\mathrm{mat}}} \tau_{\mathrm{p}} \frac{\partial \overline{U}_k}{\partial x_i} \right)^{1/2} \frac{\bar{\rho}_{\mathrm{p}} (\overline{U}_k - \overline{\overline{V_k}})}{\tau_{\mathrm{p}}} \right] \tag{4b}$$

If fluctuations of gas temperature and particle density are uncorrelated, then the averaged thermophoretic force term is,

$$\overline{\rho_{\mathrm{p}} F_{\mathrm{T},i}} = \bar{\rho}_{\mathrm{p}} \overline{\overline{F_{\mathrm{T},i}}} = \frac{K_{\mathrm{T}} \nu_{\mathrm{g}} \bar{\rho}_{\mathrm{p}}}{\tau_{\mathrm{p}}} \frac{\partial (\ln \bar{T}_{\mathrm{g}})}{\partial x_i} \tag{4c}$$

Finally, the averaged Brownian force per unit particle mass is,

$$\overline{\rho_{\mathrm{p}} F_{\mathrm{B},i}} = \bar{\rho}_{\mathrm{p}} \overline{\overline{F_{\mathrm{B},i}}} = -\frac{D_{\mathrm{B}}}{\tau_{\mathrm{p}}} \frac{\partial (\bar{\rho}_{\mathrm{p}})}{\partial x_i} \tag{4d}$$

Combining Eqs. (3a) and (3b) and substituting Eqs. (4) gives the non-conservative form of the particle momentum equation,

$$\frac{\partial \overline{\overline{V_i}}}{\partial t} + \overline{\overline{V_k}} \frac{\partial \overline{\overline{V_i}}}{\partial x_k} = \frac{\overline{U}_i - \overline{\overline{V_i}}}{\tau_{\mathrm{p}}} - \frac{\partial (\overline{\overline{v_i'' v_k''}})}{\partial x_k} + \frac{\overline{\overline{u_i'}}}{\tau_{\mathrm{p}}} - \frac{\overline{\overline{v_i'' v_k''}}}{\bar{\rho}_{\mathrm{p}}} \frac{\partial \bar{\rho}_{\mathrm{p}}}{\partial x_k} - \frac{D_{\mathrm{B}}}{\tau_{\mathrm{p}} \bar{\rho}_{\mathrm{p}}} \frac{\partial \bar{\rho}_{\mathrm{p}}}{\partial x_i} + \overline{\overline{F_{\mathrm{L},i}}} + \overline{\overline{F_{\mathrm{T},i}}} \tag{5}$$

Eq. (5) does not look very promising. In particular, the terms on the RHS with mean density gradients look out of place in a momentum equation. Nevertheless, as shown below, the equation can be recast in a form which clearly displays the various mechanisms of turbulent particle transport and also provides a suitable structure for computational work.

2.3. Particle turbulence correlations

Closure of Eq. (5) requires empirical expressions for the following correlations:

$$-\overline{\rho_{\mathrm{p}} v_i'' v_k''} = -\bar{\rho}_{\mathrm{p}} \overline{\overline{v_i'' v_k''}} \tag{6a}$$

$$\overline{\rho_{\mathrm{p}} u_i'} = \bar{\rho}_{\mathrm{p}} \overline{\overline{u_i'}} \tag{6b}$$

The correlation in Eq. (6a) is called the *particle Reynolds stress*. That in Eq. (6b) does not have a recognised name but will be referred to here as the *density–velocity correlation*.

The first stage in modelling the particle Reynolds stress is to examine its transport equation. The method of derivation is similar to the procedure for deriving the Reynolds stress transport equation in single-phase flow and has been carried through by Derevich and Zaichik (1988) and others. Neglecting lift, thermophoresis and Brownian motion, the equation is,

$$\frac{\partial(\overline{\overline{v_i'' v_j''}})}{\partial t} + \overline{\overline{V_k}} \frac{\partial(\overline{\overline{v_i'' v_j''}})}{\partial x_k} = -\frac{1}{\bar{\rho}_{\mathrm{p}}} \frac{\partial(\bar{\rho}_{\mathrm{p}} \overline{\overline{v_i'' v_j'' v_k''}})}{\partial x_k} - \overline{\overline{v_i'' v_k''}} \frac{\partial \overline{\overline{V_j}}}{\partial x_k} - \overline{\overline{v_j'' v_k''}} \frac{\partial \overline{\overline{V_i}}}{\partial x_k} + \frac{\overline{\overline{u_i' v_j''}} + \overline{\overline{u_j' v_i''}} - 2\overline{\overline{v_i'' v_j''}}}{\tau_{\mathrm{p}}} \tag{7}$$

In a *homogeneous* turbulent particle flow all gradients of mean quantities vanish and,

$$\overline{\overline{v_i'' v_j''}} = \frac{\overline{\overline{u_i' v_j''}} + \overline{\overline{u_j' v_i''}}}{2} \tag{8}$$

For inhomogeneous turbulence, the simplest approach is to ignore the stress production terms in Eq. (7) and accept Eq. (8) regardless. YL97 show that this assumption of *local equilibrium* can be surprisingly effective because it may allow the gross features to be predicted correctly even though local details are less accurate. This, after all, is about the best that can be expected from current *single-phase* turbulence calculations!

Even if Eq. (8) is accepted, however, it is still necessary to provide a local equilibrium model for $\overline{\overline{(u_i' v_j'')}}$. The simplest prescription (discussed in Appendix A) is,

$$\overline{\overline{u_i' v_j''}} = \overline{\overline{u_j' v_i''}} \cong \Gamma \overline{u_i' u_j'} \tag{9a}$$

where,

$$\Gamma = \frac{1}{\tau_{\mathrm{p}}} \int_0^\infty \mathrm{e}^{-s/\tau_{\mathrm{p}}} R(s)\, \mathrm{d}s \tag{9b}$$

$R(s)$ is the gas velocity autocorrelation function. A commonly used approximation is the simple expression $R(s) = \exp(-s/\tau_{\mathrm{g}})$ where τ_{g} is an integral time-scale of the turbulence. Substituting into Eq. (9b) gives,

$$\Gamma = \frac{\tau_{\mathrm{g}}}{\tau_{\mathrm{g}} + \tau_{\mathrm{p}}} \tag{10}$$

Finally, therefore,

$$\overline{\overline{v_i'' v_j''}} \cong \Gamma \overline{u_i' u_j'} = \frac{\tau_{\mathrm{g}}}{\tau_{\mathrm{g}} + \tau_{\mathrm{p}}} \overline{u_i' u_j'} \tag{11}$$

Eqs. (9)–(11) have been quoted by Derevich and Zaichik (1988), Simonin and Viollet (1990) and Reeks (1991). However, although Eq. (9a) clearly requires the averaging to be density-weighted, none of the derivations actually take this into account (see Appendix A).

The density–velocity correlation is also considered in Appendix A. For homogeneous turbulence, the theory relates this to the mean particle density gradient via,

$$\bar{\rho}_{\mathrm{p}}\overline{\overline{u_i'}} \cong -\Gamma D_{ik}\frac{\partial \bar{\rho}_{\mathrm{p}}}{\partial x_k} \tag{12a}$$

where D_{ik} is the turbulent diffusion tensor for a passive scalar. D_{ik} is given by,

$$D_{ik} = \tau_{\mathrm{g}}\overline{u_i'u_k'} \tag{12b}$$

and is independent of τ_{p}. Derevich and Zaichik (1988), Simonin and Viollet (1990) and Reeks (1991) all arrive at similar equations. Further simplification can be achieved by assuming isotropy so that $D_{ik} = \delta_{ik}D_{\mathrm{T}}$ where D_{T} is the isotropic turbulent diffusion coefficient. Thus,

$$\bar{\rho}_{\mathrm{p}}\overline{\overline{u_i'}} \cong -\Gamma D_{\mathrm{T}}\frac{\partial \bar{\rho}_{\mathrm{p}}}{\partial x_i} \tag{13}$$

In practice, D_{T} can be estimated from the turbulent Schmidt number $Sc_{\mathrm{T}} = \nu_{\mathrm{T}}/D_{\mathrm{T}}$ which is assumed to take values close to unity. ν_{T} is the eddy viscosity of the carrier gas flow and is assumed known throughout the flowfield. It should be noted that the correction for the effect of *crossing trajectories* suggested by Simonin et al. (1993) has not been included.

The method is completed by providing a prescription for τ_{g}. Recently, Rambaud et al. (2002) compared a number of well-known methods for estimating the Lagrangian integral time-scale in a channel-flow with DNS data. Interestingly, the accuracy of the predictions varied inversely with the complexity of the method! The most reliable approach was to obtain τ_{g} from eddy viscosity data as suggested in YL97. Thus,

$$\tau_{\mathrm{g}} \cong \frac{\nu_{\mathrm{T}}}{\overline{u_\alpha' u_\alpha'}} \tag{14}$$

The most appropriate co-ordinate direction α to use in Eq. (14) is that normal to the wall on which deposition is occurring. Further away from the wall, the value of τ_{g} is not critical.

2.4. Further development of the particle equations

Combination of Eqs. (5), (10), (11) and (12) gives the following form of the ensemble-averaged particle momentum equation,

$$\frac{\partial \overline{\overline{V_i}}}{\partial t} + \overline{\overline{V_k}}\frac{\partial \overline{\overline{V_i}}}{\partial x_k} = -\frac{\partial(\Gamma\overline{u_i'u_k'})}{\partial x_k} - \frac{(D_{\mathrm{T}} + D_{\mathrm{B}})}{\tau_{\mathrm{p}}\bar{\rho}_{\mathrm{p}}}\frac{\partial \bar{\rho}_{\mathrm{p}}}{\partial x_i} + \frac{\overline{U}_i - \overline{\overline{V_i}}}{\tau_{\mathrm{p}}} + \overline{\overline{F_{\mathrm{L},i}}} + \overline{\overline{F_{\mathrm{T},i}}} \tag{15}$$

For computational work, and also to obtain a clearer picture of the transport mechanisms, it is useful to separate the particle flux into convective and diffusive components. This is done by *defining* an ensemble-mean density-weighted convective velocity $\overline{\overline{W_i}}$ by the equation,

$$\bar{\rho}_{\mathrm{p}}\overline{\overline{V_i}} = \bar{\rho}_{\mathrm{p}}\overline{\overline{W_i}} - (D_{\mathrm{T}} + D_{\mathrm{B}})\frac{\partial\bar{\rho}_{\mathrm{p}}}{\partial x_i} \tag{16}$$

Substituting Eq. (16) into Eqs. (3a) and (15) has the effect of shifting the diffusive terms into the mass conservation equation,

$$\frac{\partial\bar{\rho}_{\mathrm{p}}}{\partial t} + \frac{\partial(\bar{\rho}_{\mathrm{p}}\overline{\overline{W_k}})}{\partial x_k} = \frac{\partial}{\partial x_k}\left[(D_{\mathrm{T}} + D_{\mathrm{B}})\frac{\partial\bar{\rho}_{\mathrm{p}}}{\partial x_k}\right] \tag{17a}$$

$$\frac{\partial\overline{\overline{V_i}}}{\partial t} + \overline{\overline{V_k}}\frac{\partial\overline{\overline{V_i}}}{\partial x_k} \cong -\frac{\partial(\Gamma\overline{u_i'u_k'})}{\partial x_k} + \frac{(\overline{U}_i - \overline{\overline{W_i}})}{\tau_{\mathrm{p}}} + \overline{\overline{F}}_{\mathrm{L},i} + \overline{\overline{F}}_{\mathrm{T},i} \tag{17b}$$

Eq. (17a) has the form of a conventional convection–diffusion equation. The diffusivity D_{T} is independent of τ_{p}. This is because, although high inertia particles respond poorly to the gas turbulence, their induced velocities are more persistent than those of low inertia particles. This result has been confirmed by Reeks (1977) and Pismen and Nir (1978).

When τ_{p} is small, the main component of the particle flux is diffusive and Eq. (16) shows that there is substantial difference between $\overline{\overline{V_i}}$ and $\overline{\overline{W_i}}$. But, in such situations, the acceleration term on the LHS of Eq. (17b) can usually be neglected because, compared with $\overline{U}_i - \overline{\overline{W_i}}$, it is multiplied by τ_{p}. When τ_{p} is large, the acceleration term is definitely non-negligible, but then the particle flux is mainly convective and $\overline{\overline{V_i}} \cong \overline{\overline{W_i}}$. This argument suggests that it is possible to replace the total velocity $\overline{\overline{V_i}}$ *in the acceleration term* by the convective velocity $\overline{\overline{W_i}}$ without serious error over the whole range of τ_{p}. Eq. (17b) then becomes,

$$\frac{\partial\overline{\overline{W_i}}}{\partial t} + \overline{\overline{W_k}}\frac{\partial\overline{\overline{W_i}}}{\partial x_k} \cong -\frac{\partial(\Gamma\overline{u_i'u_k'})}{\partial x_k} + \frac{(\overline{U}_i - \overline{\overline{W_i}})}{\tau_{\mathrm{p}}} + \widetilde{F}_{\mathrm{L},i} + \widetilde{F}_{\mathrm{T},i} \tag{17c}$$

Eq. (17c) is very instructive. The left hand side represents the mean particle convective acceleration while the terms on the right represent the forces per unit particle mass producing this acceleration. The final three terms represent drag, lift and thermophoresis. The first term involving the particle Reynolds stress deserves further comment.

Consider a 2D boundary layer type flow with the wall parallel to the x_1-direction and suppose that all terms in the wall-normal (x_2-direction) particle momentum equation can be neglected except for the viscous drag and the Reynolds stress term. Eq. (17c) reduces to,

$$\bar{\rho}_{\mathrm{p}}\overline{\overline{V_2}} = -\tau_{\mathrm{p}}\bar{\rho}_{\mathrm{p}}\frac{\partial(\overline{\overline{v_2''v_2''}})}{\partial x_2} = -\tau_{\mathrm{p}}\bar{\rho}_{\mathrm{p}}\frac{\partial(\Gamma\overline{u_2'u_2'})}{\partial x_2} \tag{18}$$

Eq. (18) highlights the fact that the gradient of the *wall-normal component* of the particle Reynolds stress causes a drift flux of particles towards the wall. This is known as *turbophoresis* (Reeks, 1983) and, as shown by YL97, is the dominant transport mechanism when $\tau_{\mathrm{p}} \approx \tau_{\mathrm{g}}$. Particles impelled towards the wall by eddies in the buffer layer coast into the sub-layer from where they are unable to return because the turbulent fluctuations are, *on average*, too small.

Neglect of turbophoresis can result in errors of several orders of magnitude in predicted deposition rates.

2.5. The status of particle turbulence modelling

It is interesting to note that Eqs. (17), which have been derived using density-weighted averaging, are essentially the same equations obtained in YL97 using the non-density-weighted approach. In YL97, however, a correlation involving the divergence of the particle velocity field was ignored. This term is related to the compressibility of the particle–fluid and does not appear in the present analysis because it is absorbed by the density-weighting. Now, the magnitude of the correlation in question has recently been estimated by Cerbelli et al. (2001) who claim that it can have a significant effect on deposition rates. This, in turn, suggests that there may be an inconsistency of comparable magnitude in the density-weighted turbulence modelling which has not previously been noted. Further investigation points to the simple model of Eq. (9a) which is probably a better representation of $\overline{\overline{(u_i'v_j')}}$ rather than $\overline{\overline{(u_i'v_j'')}}$, the term actually required. The analysis in Appendix A, which is a formal derivation of Eq. (9a), emphasises the assumptions and helps to substantiate this view.

Although the particle turbulence model used in the present work is simple and straightforward, the authors are aware that considerably more elaborate models have been proposed. For example, Simonin et al. (1993) have derived transport equations for the density–velocity correlation of Eq. (6b) and the gas–particle velocity covariance of Eq. (8). When these are integrated along with Eq. (7), the local equilibrium assumption can be dropped in favour of closure at a higher level. Simonin et al. (1997) claim improved accuracy but their calculations only cover a small range of particle response times.

In the opinion of the authors, the current state of particle turbulence theory is such that more complex modelling should be introduced only when it can be reliably substantiated, preferably by experimental data. The theory of particle turbulence is extremely approximate and it is important to appreciate that the reliability of even supposedly well-established results is still questionable. The expectation of improved accuracy by more complex modelling and closure at higher levels may not be well-founded.

3. Numerical solution procedure

Eq. (17c) does not involve the particle density and can be solved for $\overline{\overline{W_i}}$ independently of Eq. (17a). This is useful for certain applications but, for the finite-volume numerical solution procedure described below, it is actually preferable to work with a conservative form of the particle momentum equation while retaining the diffusive terms in the mass conservation equation. This can be achieved by combining Eq. (3a) with (17b) before making the approximation $\overline{\overline{W_i}} \cong \overline{\overline{V_i}}$ in the acceleration term. The resulting pair of equations which serve as a basis for the numerical solution procedure are therefore,

$$\frac{\partial \bar{\rho}_\mathrm{p}}{\partial t} + \frac{\partial (\bar{\rho}_\mathrm{p} \overline{\overline{W_k}})}{\partial x_k} = \frac{\partial}{\partial x_k}\left[(D_\mathrm{T} + D_\mathrm{B}) \frac{\partial \bar{\rho}_\mathrm{p}}{\partial x_k} \right] \tag{19a}$$

$$\frac{\partial(\bar{\rho}_{\mathrm{p}}\overline{\overline{W_i}})}{\partial t}+\frac{\partial(\bar{\rho}_{\mathrm{p}}\overline{\overline{W_i W_k}})}{\partial x_k}\cong\bar{\rho}_{\mathrm{p}}\left[-\frac{\partial(\Gamma\overline{u_i' u_k'})}{\partial x_k}+\frac{(\overline{U}_i-\overline{\overline{W_i}})}{\tau_{\mathrm{p}}}+\overline{\overline{F_{\mathrm{L},i}}}+\overline{\overline{F_{\mathrm{T},i}}}\right] \tag{19b}$$

A finite-volume scheme is used and the 2D versions of Eqs. (19) are discretised on a mesh of arbitrarily shaped quadrilaterals as shown in Fig. 1a. A pseudo-transient numerical method is used, similar to that described by Slater and Young (2001) for non-turbulent flows. The following brief description highlights those aspects concerned with turbulent transport.

Cell-centred storage is used with a second-order accurate, symmetrical discretisation for the fluxes through the cell faces. The second-order derivatives in Eq. (19a) are constructed as follows. Referring to Fig. 1b, and denoting the co-ordinates by (x,y), the first-order derivatives of a variable ϕ at the centre of cell ABCD are given by (Hirsch, 1990),

$$\left(\frac{\partial\phi}{\partial x}\right)=\frac{(\phi_{\mathrm{A}}-\phi_{\mathrm{C}})(y_{\mathrm{B}}-y_{\mathrm{D}})-(\phi_{\mathrm{B}}-\phi_{\mathrm{D}})(y_{\mathrm{A}}-y_{\mathrm{C}})}{(x_{\mathrm{A}}-x_{\mathrm{C}})(y_{\mathrm{B}}-y_{\mathrm{D}})-(x_{\mathrm{B}}-x_{\mathrm{D}})(y_{\mathrm{A}}-y_{\mathrm{C}})} \tag{20a}$$

$$\left(\frac{\partial\phi}{\partial y}\right)=\frac{(\phi_{\mathrm{B}}-\phi_{\mathrm{D}})(x_{\mathrm{A}}-x_{\mathrm{C}})-(\phi_{\mathrm{A}}-\phi_{\mathrm{C}})(x_{\mathrm{B}}-x_{\mathrm{D}})}{(x_{\mathrm{A}}-x_{\mathrm{C}})(y_{\mathrm{B}}-y_{\mathrm{D}})-(x_{\mathrm{B}}-x_{\mathrm{D}})(y_{\mathrm{A}}-y_{\mathrm{C}})} \tag{20b}$$

If the ϕ's are themselves first-order derivatives at the points A, B, C and D, then Eqs. (20) allow the calculation of the second-order derivatives at the central point.

The symmetrical discretisation places equal weight upon upstream and downstream travelling information which is counter to the convective nature of the flow. Numerical stability is therefore maintained by adding adjustable artificial diffusion as described by Slater and Young (2001). It is important that this artificial diffusion is directionally dependent. The wall-normal deposition fluxes are much lower than the streamwise fluxes and are easily swamped by isotropic artificial diffusion.

As discussed by Slater and Young (2001), the correct formulation of physically-based boundary conditions is vital to successful flow calculations. At the inlet boundary, ρ_{p} and the $\overline{\overline{W_i}}$

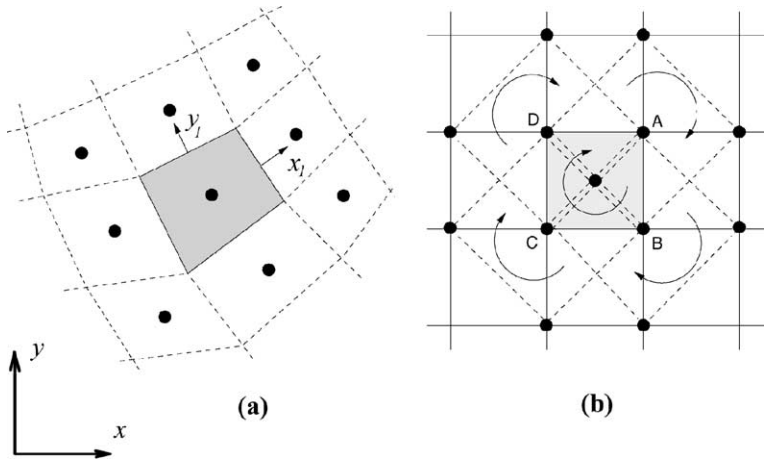

Fig. 1. (a) Structured mesh of arbitrarily shaped quadrilaterals, cell-centred storage. (b) Twelve point stencil used to calculate second derivatives.

are prescribed. At solid wall and outflow boundaries the particle flux is calculated by Eq. (16) as the sum of the convective and diffusive contributions. When the convective velocity vector is directed out of the flow, the convective flux is calculated using a first-order upwinding scheme which models the physics correctly. The diffusive wall fluxes, on the other hand, are associated with an upstream influence and are evaluated from the particle density field with boundary condition $\rho_p = 0$. This condition, although physically incorrect even in the limit $\tau_p \to 0$ (YL97), is easy to implement and the numerical errors are small.

4. Deposition from 2D turbulent channel-flow

4.1. Experimental data and non-dimensionalisation

Virtually all the experimental data on particle deposition has been obtained in turbulent pipe-flow while the calculation method described above is currently restricted to plane 2D flows. However, because deposition is mainly controlled by the near-wall turbulence, calculations for channel-flow, non-dimensionalised with respect to wall variables, should give similar results to pipe-flow and provide a suitable vehicle for code validation.

Pipe-flow deposition data are usually presented by plotting dimensionless particle deposition velocity V_{dep+} against dimensionless relaxation time τ_{p+}. These are defined by,

$$V_{dep+} = \frac{J_w}{u_\tau \bar{\rho}_{p,mean}} \qquad \tau_{p+} = \frac{\tau_p u_\tau^2}{\nu_g} \tag{21}$$

where J_w is the deposition mass flux, u_τ is the friction velocity, $\rho_{p,mean}$ is the mean particle density in the pipe and ν_g is the gas kinematic viscosity. V_{dep+} is independent of streamwise position if the fluid and particle flows are both fully-developed (YL97). The graph of V_{dep+} versus τ_{p+} is not universal because, for $\tau_{p+} \ll 1$, V_{dep+} becomes independent of τ_{p+} and depends only on the Schmidt number ($Sc = \nu_g D_B$). In this region data are usually presented in terms of the group $(\tau_{p+}/Sc^2)^{1/3}$ which is independent of particle diameter. Fig. 2 shows a compilation of some experimental data.

4.2. The fluid flowfield and computational grid

The mean streamwise fluid velocity profile was expressed by $\bar{u}_{x+} = f(y_+)$, where x is streamwise distance, y is distance from the wall and + denotes non-dimensionalisation using wall variables. The empirical expression of Kallio and Reeks (1989) was used. The eddy viscosity ν_T and the dimensionless wall-normal mean-square fluctuating velocity $\overline{(u'_{y+}u'_{y+})}$ were assumed to depend on y_+ only. The equations of YL97 were used. $\overline{(u'_{x+}u'_{x+})}$ is of secondary importance and was obtained assuming isotropy of the turbulence.

Calculations were performed for a 2D channel of height 10 mm carrying air at a Reynolds number of 4000. The channel length depended on the particle inertia. Thus, for $\tau_{p+} = 0.01$ a length of 0.1 m was sufficient to attain fully-developed particle profiles while for $\tau_{p+} = 1000$, 1.3 m was required. For computational accuracy, a separate grid was used for each particle size, experience showing that about 20 streamwise and 30 cross-channel cells were sufficient. Across the

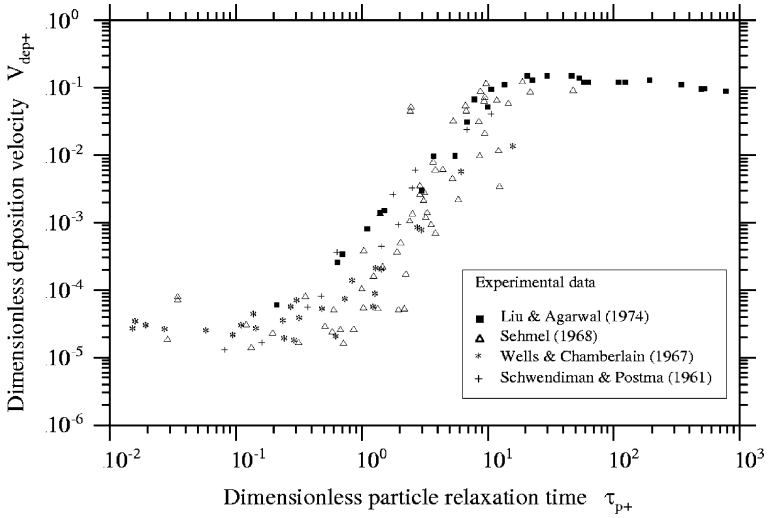

Fig. 2. Particle deposition from fully-developed turbulent pipe-flow: A compilation of isothermal experimental data.

channel, a non-uniform grid was used with a very fine spacing near the wall. The first point was at a distance of one particle radius from the wall and the rest of the grid established using a geometric progression with ratio 1.3 or less.

4.3. Attainment of fully-developed particle flow

At the inlet, the particles were injected computationally with a uniform distribution and after a certain distance the flow became self-similar. The dimensionless deposition flux V_{dep+} and the particle mean velocity profile were then independent of axial location but $\bar{\rho}_p$ continued to fall because of deposition. The non-dimensional density $\bar{\psi} = \bar{\rho}_p/\bar{\rho}_{p,mean}$ remained constant, however. ($\bar{\rho}_{p,mean}$ is the particle density averaged across the channel.) Fig. 3 shows results for particles with $\tau_{p+} = 200$. Fig. 3a is a scale drawing of the pipe while Fig. 3b shows the grid, stretched so that the overall aspect ratio is one. Fig. 3c presents contours of $\bar{\rho}_p$ ($\bar{\rho}_p = 1$ at inlet) which fall continually in the flow direction and Fig. 3d shows contours of $\bar{\psi}$ becoming independent of axial distance half way along the pipe.

The ability to calculate deposition in the developing flow region is not taken further here although it is of engineering interest and also useful for interpreting experimental data. For example, there is at present no information available on the distance required to obtain a fully-developed particle flow in a pipe or channel.

4.4. Results for isothermal flow

Initially, the gas flow was assumed to be isothermal and thermophoresis was neglected. Particle deposition is then controlled by turbulent and Brownian diffusion, turbophoresis, viscous drag, and shear-flow lift. It was assumed in all calculations that solid boundaries are perfectly absorbing and hence that impaction and deposition are synonymous.

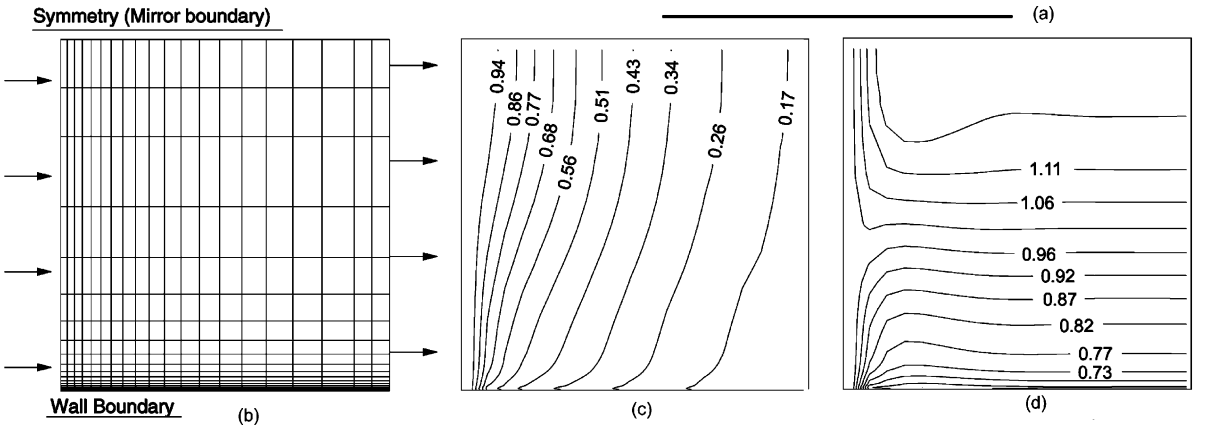

Fig. 3. Particle density in isothermal turbulent channel-flow with $\tau_{p+} = 200$. (a) Channel to scale, aspect ratio = 224, (b) computational grid stretched in wall-normal direction, aspect ratio = 1, (c) contours of $\bar{\rho}_p$, (d) contours of $\bar{\psi} = \bar{\rho}_p/\bar{\rho}_{p,mean}$.

When $\tau_{p+} < 0.1$, turbulent and Brownian diffusion dominate and convective transport is unimportant. Turbulent diffusion dominates in the core and buffer regions but, very close to the wall, the transport is by Brownian diffusion. Fig. 4 shows the results of the 2D calculations obtained by setting $(\tau_{p+}/Sc^2)^{1/3} = 5 \times 10^{-5}$ and 'turning off' the convective terms. Also plotted are the experimental data [for which $(\tau_{p+}/Sc^2)^{1/3} = 5 \times 10^{-5}$ is approximately representative] and an analytical solution calculated by the method of Beal (1970). The agreement, particularly with the analytical solution, is very good.

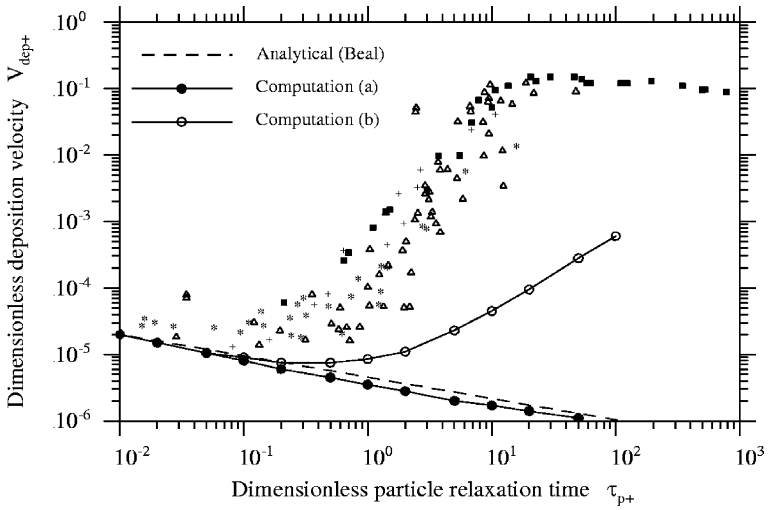

Fig. 4. Deposition from isothermal turbulent channel-flow. Calculations include turbulent and Brownian diffusion only. Experimental data as for Fig. 2. (a) Particles treated as point masses, (b) boundary offset by one particle radius.

Fig. 4 also shows the effect of displacing the boundary by an *interception distance* of one particle radius. It is evident, however, that the steep rise in the deposition curve is caused not by this but rather by the effects of turbophoresis. Fig. 5 shows the results of calculations including turbophoresis, diffusion and viscous drag, with and without the addition of lift. For the calculations without lift, the prediction for $\tau_{p+} > 100$ is good but, in the region $1 < \tau_{p+} < 10$, the curve rises less steeply than the experimental data. The introduction of lift makes a substantial improvement. The particles lead the carrier fluid near the wall resulting in a wallwards directed lift force, the magnitude of which depends on the slip velocity. The effect is most marked in the range $10 < \tau_{p+} < 100$ but, even with lift, the predicted deposition rates are still low compared with the experimental data.

A comparison with the pipe-flow calculations of YL97 (Fig. 7 of that paper) shows that the addition of lift produces similar changes to those shown in Fig. 5 but that the agreement with the experimental data is superior. This is probably because the present calculations were performed for a plane 2D channel rather than an axi-symmetric pipe and that deposition rates for $\tau_{p+} \approx 10$ are very sensitive to small variations in the modelling parameters.

The variations of particle velocity and density with y_+ are shown in Fig. 6 for $\tau_{p+} = 0.1$, 1, 50, 100 and 1000. The effect of lift is included. On the left is the particle mean streamwise velocity $\overline{\overline{W}}_{x+}$. The value at the wall increases with τ_{p+} because particles do not obey a no-slip condition. The wall-normal particle velocity $\overline{\overline{W}}_{y+}$ is shown in the centre. The negative peak at $y_+ \cong 15$ for $\tau_{p+} = 0.1$ and 1 corresponds to the maximum turbophoretic force. For $\tau_{p+} = 50$, 100 and 1000, the effect of lift is clearly seen as the particles continue to accelerate towards the wall despite the reduction of the turbophoretic force in the region $y_+ < 15$.

Profiles of non-dimensional particle density $\bar{\psi}$ are shown on the right of Fig. 6. For $\tau_{p+} = 0.1$ turbulent and Brownian diffusion dominate. The very steep gradient in $\bar{\psi}$ at the wall is necessary

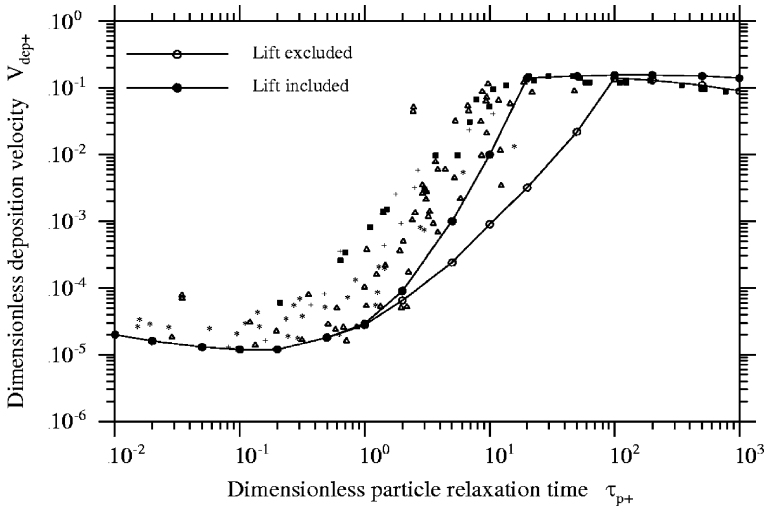

Fig. 5. Deposition from isothermal turbulent channel-flow with and without shear-flow lift. Calculations include turbulent diffusion, turbophoresis, viscous drag, Brownian diffusion and shear-flow lift as indicated. Experimental data as for Fig. 2.

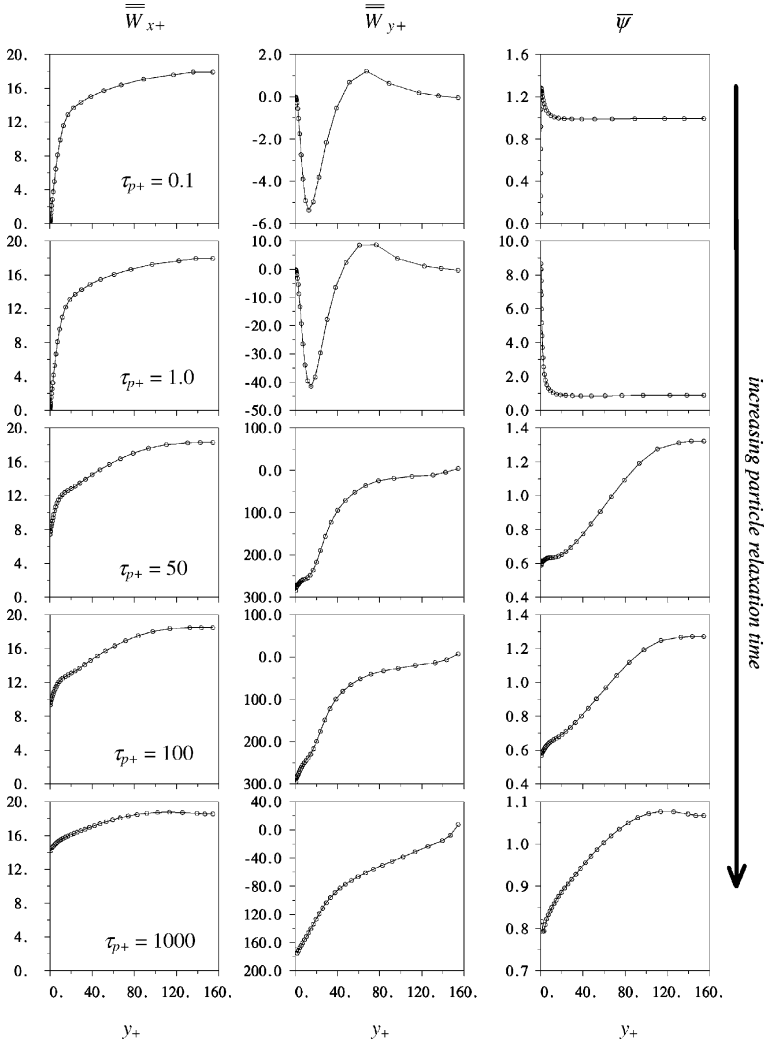

Fig. 6. Deposition from isothermal turbulent channel-flow. Calculations include turbulent diffusion, turbophoresis, viscous drag, shear-flow lift and Brownian diffusion. Particle streamwise velocity (left), particle wall-normal convective velocity (centre), particle density (right). All quantities are non-dimensionalised. Note the changes of ordinate scale from top to bottom.

to maintain the particle flux by Brownian diffusion when the fluid turbulence level is very low. For $\tau_{p+} = 1$, the high peak in $\bar{\psi}$ is probably non-physical and stems from the assumption of local homogeneous turbulence. In reality, the particle fluctuating velocity would not be completely attenuated as the particles approach the wall and turbophoresis would remain an active transport mechanism right through the sub-layer. For $\tau_{p+} = 50$, 100 and 1000, $\bar{\psi}$ is of order unity everywhere and is non-zero at the wall. The variations with y_+ are related to convective continuity requirements and do not indicate high diffusive fluxes.

A comparison of Fig. 6 with the similar Fig. 10 of YL97 shows that, although there is good qualitative agreement in terms of the shape of the profiles, significant quantitative differences

exist. Evidently, the detailed particle turbulence field is very sensitive to small changes in the modelling assumptions and quantitative predictions should be treated cautiously. This, of course, is not unlike the current status of *single-phase* turbulent boundary layer calculations where good predictions of the wall shear stress can often be made, despite an inability to resolve all details of the near-wall turbulence.

4.5. Results for non-isothermal flow

When the channel wall is heated or cooled, cross-stream temperature gradients generate thermophoretic forces on the particles which can be very significant in modifying the deposition rates. In particular, if the wall is cooled below the mean gas temperature, thermophoresis enhances the deposition rate. It is not the purpose of this paper to describe an exhaustive study of thermophoresis but it is of interest to present some preliminary results.

Fig. 7 shows the results of calculations where all transport mechanisms, including thermophoresis, have been included. ΔT is the difference between the gas temperatures on the centre-line and on the wall. The experimental measurements were obtained by Leeming (1995) using equipment similar to that of Liu and Agarwal (1974) but with a heated gas–particle flow and a cooled pipe wall. For the calculations, the thermophoretic coefficient K_T of Eq. (2c) corresponded to the value in the experiments. From Fig. 7, it is clear that small temperature differences can have a dramatic effect on deposition rates for low inertia particles. Thus, when $\Delta T = 10$ K, the deposition rate of particles with $\tau_{p+} = 0.1$ increases by two orders of magnitude. The experimental data, although sparse, are in good agreement with the calculations, thus bestowing a certain credibility on the theory. A more detailed study of the effects of thermophoresis on particle deposition from turbulent flows is currently in progress.

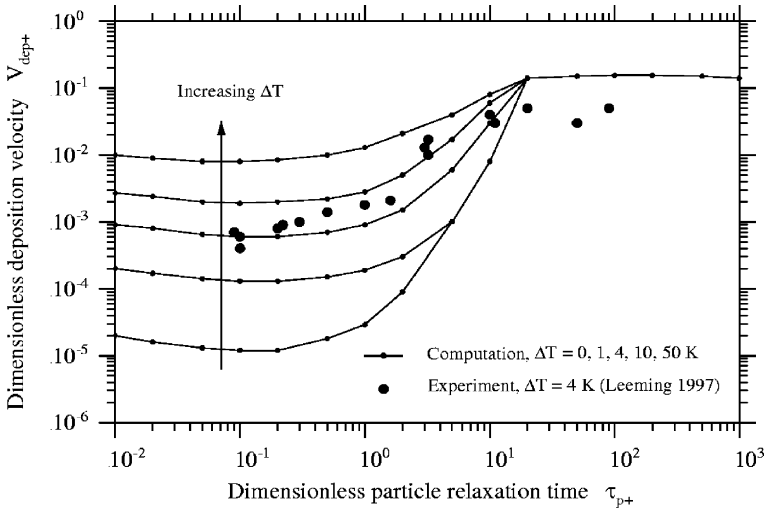

Fig. 7. Deposition from non-isothermal turbulent channel-flow including thermophoresis. Calculations include turbulent diffusion, turbophoresis, viscous drag, shear-flow lift, Brownian diffusion and thermophoresis.

5. Particle transport in boundary layers

Although not a complete validation, the results of the previous section provide good evidence (i) that deposition rates in the only flow situation where experimental data exists can be predicted with reasonable accuracy and, (ii) that the calculation scheme can handle ranges of particle response times and deposition rates extending over four or five orders of magnitude. On the strength of this, more complex geometries were considered, in particular the gas–particle flow in a 2D turbine blade cascade. This configuration is of engineering importance because of applications in predicting the deposition rates of small water droplets onto steam turbine blades and of ash particles onto blading in coal-fired gas turbines. At present, there is no reliable theoretical way of obtaining this information.

Particle flow in a cascade is also a good theoretical test case because all modes of transport are represented. When the particles enter the cascade, the velocity slip caused by the curved streamlines results in a particle drift towards the pressure surface boundary layer. Transport within the boundary layer then depends on the particle inertia, the gas velocity profile, the turbulence structure and the streamline curvature. There are two limiting cases:

(i) The particles have sufficient wallward momentum to coast across the boundary layer without being influenced strongly by the gas flow, and,
(ii) the particles are decelerated and turned by the gas in a direction parallel to the surface.

Particles with large inertia entering the boundary layer with large velocity slip will be little influenced by the turbulence and will behave more like the first limiting case, coasting across the layer to impact the surface. Particles with smaller inertia will behave more like the second limiting case and, once entrained in the boundary layer, will be influenced by all the turbulent transport mechanisms operating there.

It is therefore evident that the transport of particles in a well-defined boundary layer provides the possibility of studying some physical phenomena which are not found in channel-flow. Accordingly, the air-particle flow in a turbulent boundary layer on a flat plate with zero pressure gradient was investigated before attempting a more complex 2D cascade calculation.

5.1. The boundary layer flowfield

The flowfield was generated by the boundary layer code STAN5 developed at Stanford University. A k–l turbulence model was used and the fluctuating velocity components calculated assuming isotropy of the turbulence. This obviously limits the accuracy of the deposition calculations but the point of the exercise was to obtain physical understanding. The boundary layer was fully turbulent from the leading edge with a free-stream velocity of 100 m/s and a Reynolds number per unit length of 5.5×10^6. Fig. 8 shows contour plots of the time-mean streamwise velocity $\overline{U}_x$, the eddy viscosity ν_T and the wall-normal rms fluctuating velocity $(u'_y)_{rms} = (\overline{u'_y u'_y})^{1/2}$, together with profiles of each variable at the final x-station (normalised with respect to wall variables). At the leading edge, some 200 mm are needed for the calculation to settle down after the initial guess but, thereafter, the variables are well-behaved apart from a small 'glitch' in $(u'_y)_{rms}$ near the outer edge of the layer.

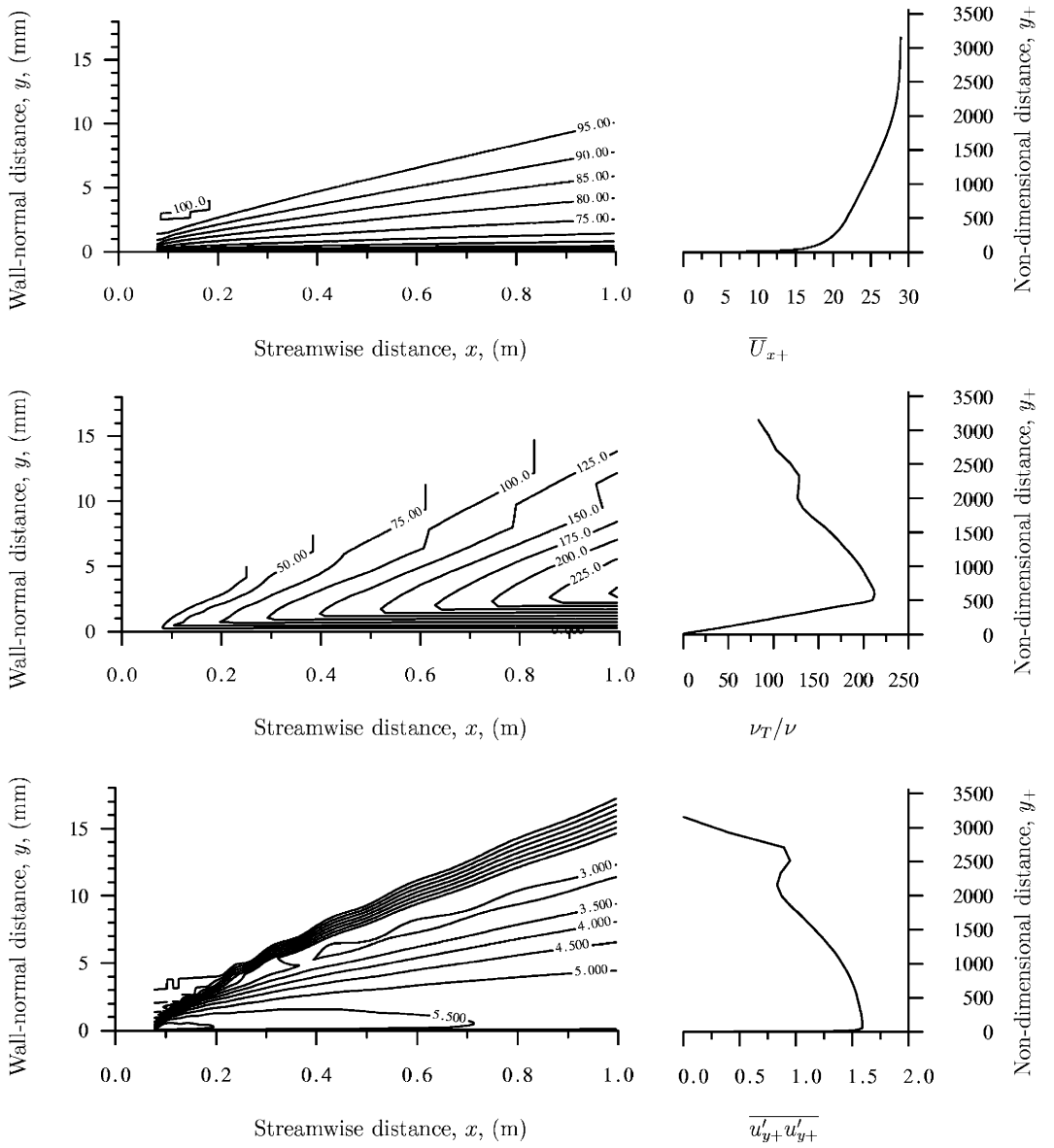

Fig. 8. Gas flowfield in a turbulent boundary layer on a flat plate with zero pressure gradient. Streamwise velocity (top), turbulent/laminar viscosity (middle), wall-normal mean-square fluctuating velocity (bottom). Profiles are at $x = 1$ m and are normalised using wall variables. Note the highly exaggerated wall-normal scale.

Fig. 8 emphasises the fact that the damping of the turbulence quantities by the wall is restricted to a very narrow physical region indeed. This is especially true for $(u'_y)_{\mathrm{rms}}$, the gradient of which is responsible for turbophoresis. $(u'_y)_{\mathrm{rms}}$ increases slowly from the free-stream boundary to a maximum at the edge of the buffer layer before dropping rapidly to zero at the wall. Over most of the

boundary layer the main mechanism of *turbulent* particle transport is diffusion. Only very close to the wall does turbophoresis play an important rôle.

5.2. Particle flow calculations

The importance of particle slip at the outer edge of the boundary layer was investigated in two calculations. The chosen particle diameters were 6 and 20 μm and the particle material density was 930 kg/m^3. As the boundary layer grows, the friction velocity u_τ changes and the dimensionless particle response time τ_{p+} increases. At the final x-station, the respective values of τ_{p+} were 82 and 892.

The particle calculations were started 200 mm from the leading edge where the boundary layer flowfield was deemed to be 'clean'. At the first x-station the slip velocity was set to zero and the particle density was assumed to be uniform across the layer. At the outer edge of the boundary layer, the *speed* of the particles was set to 100 m/s but they were injected into the layer at an angle of 30° to the plate. There was therefore a slip velocity in both the streamwise and wall-normal directions. The particle density in the free-stream was assumed to be uniform.

5.3. Behaviour of 6 μm diameter particles

Fig. 9 shows the results for the 6 μm particles. The particles enter the boundary layer at an angle of 30° with a large slip velocity and are decelerated by viscous drag. This is a laminar effect and turbulent transport is unimportant here. Fig. 9 shows profiles, at the final x-station, of the wall-normal and streamwise components of the particle convective and gas velocities and the particle density. Here, the outer edge of the boundary layer is at $y_+ \approx 3200$ and the slip velocity has been almost completely annihilated by $y_+ \approx 2000$. During the deceleration, the particle density increases (for continuity reasons) by a factor of 30.

A graphic illustration of the particle behaviour can be obtained by plotting the ensemble-mean particle pathlines. These are obtained by integrating the *total* particle velocity $\overline{\overline{V_i}}$ from Eq. (16) along chosen particle pathlines. The ensemble-mean particle mass flowrate between any two pathlines then remains constant. Selected pathlines (with a grossly exaggerated wall-normal scale) are shown in Fig. 9. The deceleration is evident as the pathlines turn towards the gas flow direction and the increasing particle density is shown by the pathline convergence.

In contrast, the behaviour near the wall is dominated by the turbulence. From $y_+ \approx 2000$ to $y_+ \approx 100$ the main form of transport *towards the wall* is turbulent diffusion. This is evident from the strong particle density gradient coupled with a near-zero convective velocity. From $y_+ \approx 100$ to the wall, the particles experience a strong turbophoretic force. This is shown by the ensemble-mean pathlines which indicate quite a strong wallward acceleration close to the wall.

For this example, the ratio of the particle flux at the wall to the flux entering the boundary layer takes the value 0.205. This highlights the strong decelerating and turning effect of the boundary layer: most particles are convected by the gas out of the downstream flow boundary.

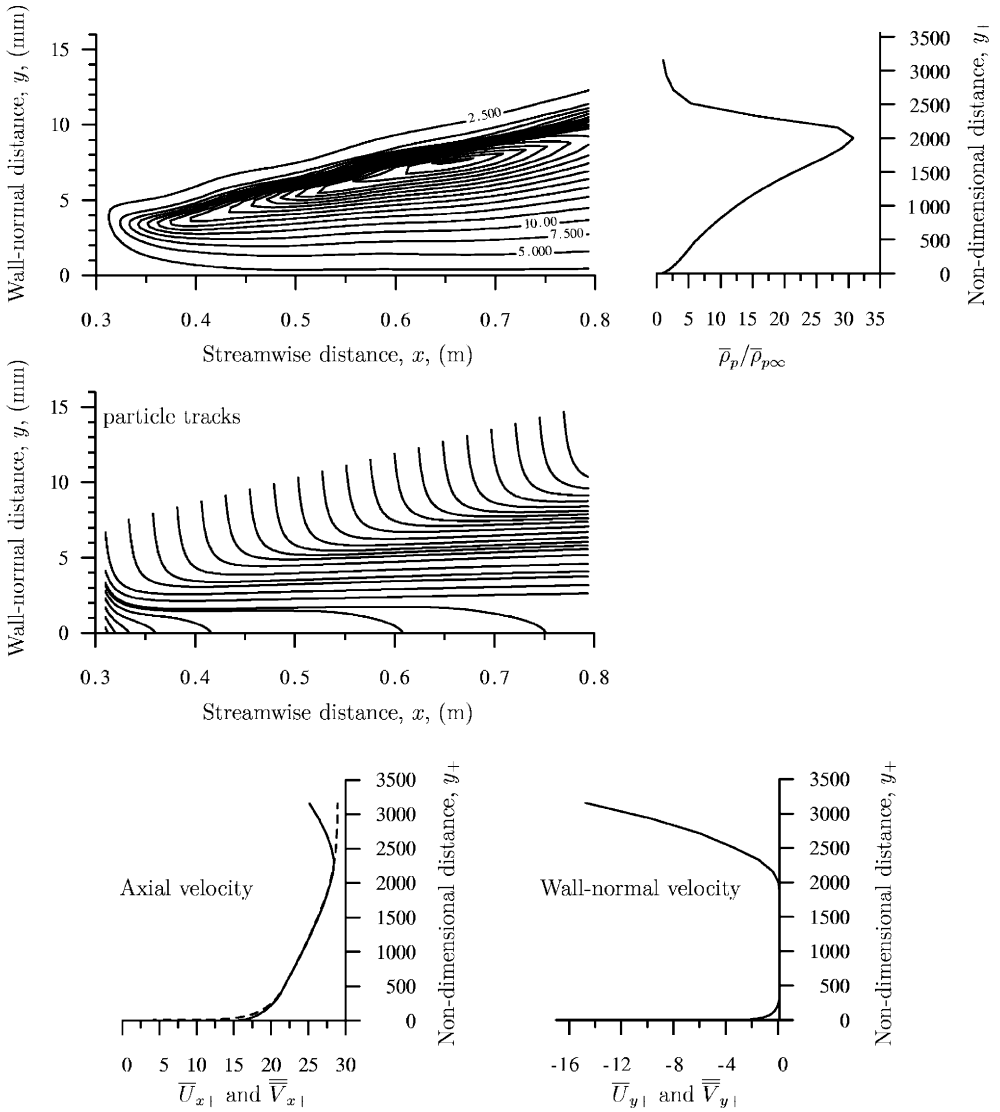

Fig. 9. Transport of 6 μm diameter particles in the turbulent boundary layer of Fig. 8. Particles are injected into the layer at an angle of 30° to the plate. Particle density normalised by free-stream value (top), ensemble-mean particle pathlines (middle), ensemble-mean streamwise and wall-normal velocities normalised by u_τ (bottom). Solid lines are particles, dashed lines are gas. Note the highly exaggerated wall-normal scale.

5.4. Behaviour of 20 μm diameter particles

The behaviour of 20 μm particles, shown in Fig. 10, is more straightforward. These particles are also injected at an angle of 30° and experience a deceleration in the y-direction due to viscous drag. There is, however, little effect on the particle velocity in the x-direction (the gas leads the particles in the free-stream but lags at the wall) and the particles experience only a mild turning

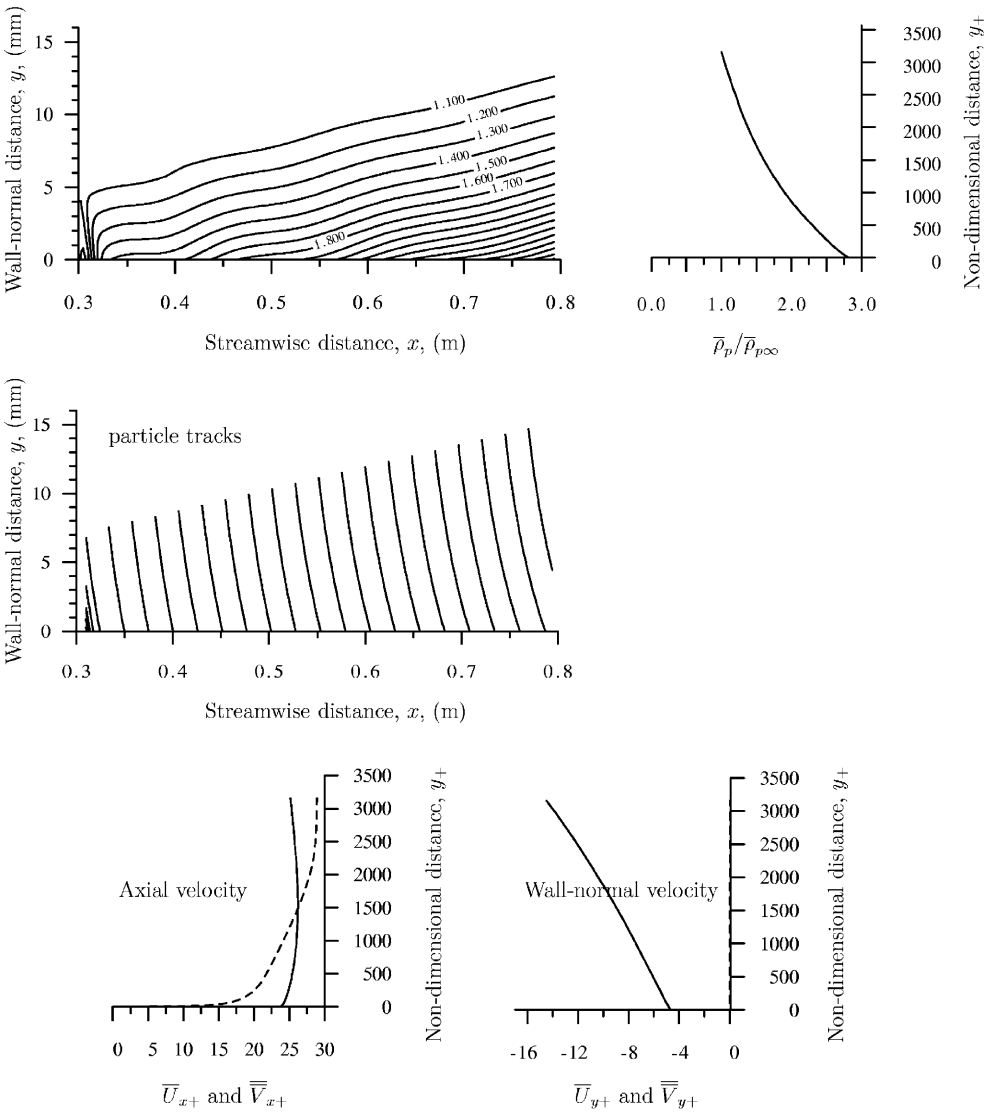

Fig. 10. Transport of 20 μm diameter particles in the turbulent boundary layer of Fig. 8. Particles are injected into the layer at an angle of 30° to the plate. Particle density normalised by free-stream value (top), ensemble-mean particle pathlines (middle), ensemble-mean streamwise and wall-normal velocities normalised by u_τ (bottom). Solid lines are particles, dashed lines are gas. Note the highly exaggerated wall-normal scale.

effect before impacting the wall. Nonetheless, the increase in particle density as required by mass continuity as the wall-normal velocity decreases is significant.

Because of the higher particle inertia, turbulent transport effects are not much in evidence. Indeed, the increasing particle density *towards* the wall actually causes a turbulent diffusive flux *away* from the wall. Its magnitude is, however, very much less than the wallwards convective

flux. The contribution from turbophoresis is also small, the high values of τ_{p+} resulting in a small value of Γ from Eq. (10).

In contrast to the 6 μm particles, the ratio of the particle mass flux impacting the plate to the flux entering the boundary layer is 0.916. Only a small fraction of the particles is convected through the downstream flow boundary.

6. Deposition in a turbine cascade

6.1. Grid generation and flowfield calculation

The complex geometry of a turbine cascade poses a number of difficult computational problems, not least the capture of particle-free zones and the accurate representation of particle density

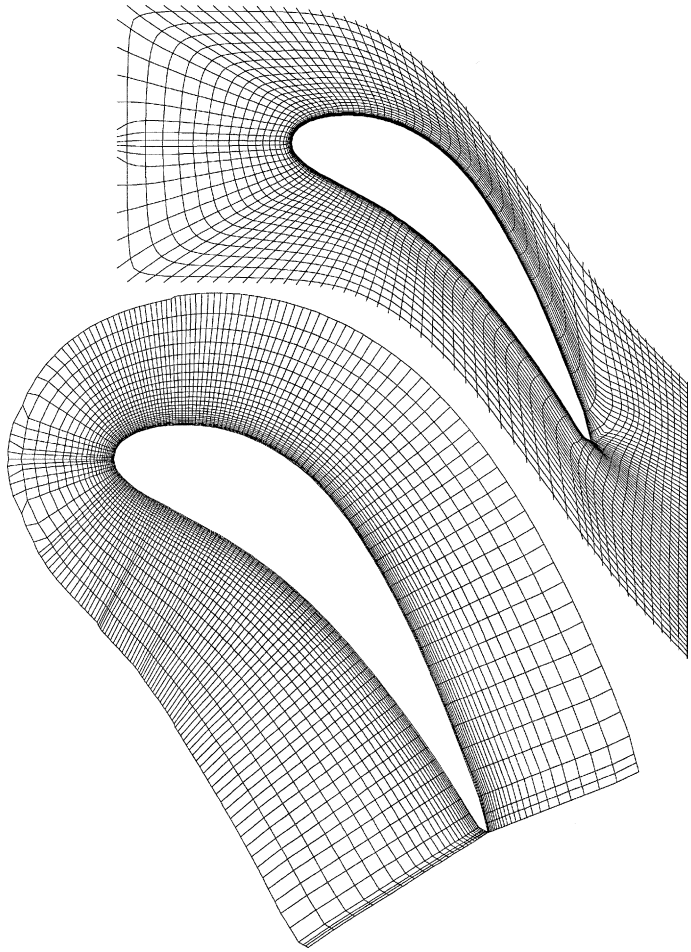

Fig. 11. Computational C-mesh for turbine blade calculation, chord length 37 mm, maximum Mach number 0.6. The lower diagram shows the near-wall mesh expanded 20 times in the wall-normal direction.

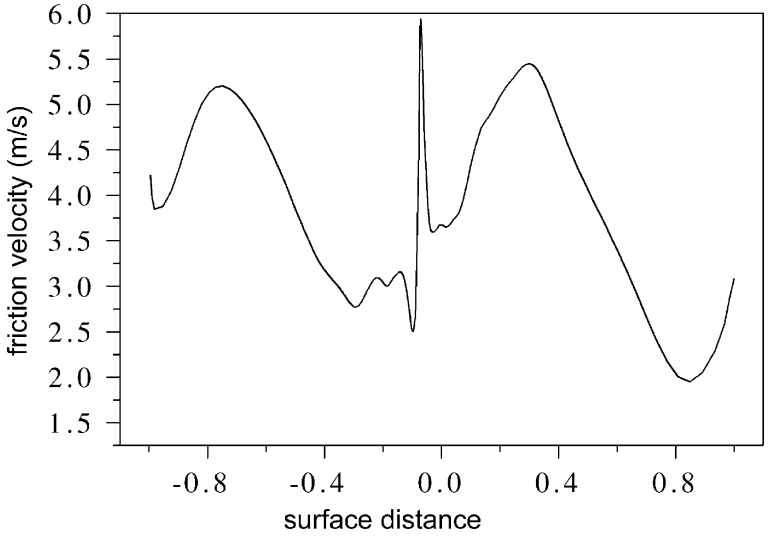

Fig. 12. Variation of friction velocity u_τ around the turbine blade. The surface distance (normalised by the total surface length) is measured from the leading edge, positive on suction surface, negative on pressure surface.

discontinuities at the zone boundaries. For turbulent flows must be added the problems of calculating deposition rates which, as exemplified by the channel-flow calculations of Section 4, may vary by several orders of magnitude.

Fig. 11 shows the turbine blade (axial chord length 37 mm, maximum Mach number 0.6) selected for analysis. The blade was designed for use in a coal-fired industrial gas turbine. Although the gas stream is filtered, ash particles of diameter 5–10 μm enter the turbine and it is important to be able to predict their rate of deposition onto the blades. The gas temperature at inlet is 1500 K but the blades are cooled to a surface temperature 400 K lower. Such a large temperature difference suggests that thermophoresis may be important.

The gas velocity field was calculated using a Navier–Stokes solver. The velocities were then interpolated onto the C-mesh of Fig. 11 for the particle calculations. Using the computed blade surface pressure distribution, a boundary layer code was used to generate the required turbulence correlations. The boundary layer was assumed to be turbulent from the forward stagnation point and the variation of the friction velocity u_τ is shown in Fig. 12.

6.2. Deposition characteristics for 5 μm diameter particles

Fig. 13 shows particle density contours (normalised by the value at cascade inlet) for particles of diameter 5 μm entering the cascade uniformly with zero slip velocity. There is a particle-free region adjacent to the suction surface caused by the inability of the particles to follow the gas streamlines. The method by which such zones are automatically captured at run-time is described by Slater and Young (2001).

Fig. 14 shows the variation of deposition rate on the blade surface for four different calculations. The total area under each curve is related to the *deposition fraction F*, defined as the fraction of particles entering the cascade which deposit (F is presented as a percentage in Fig. 14). When

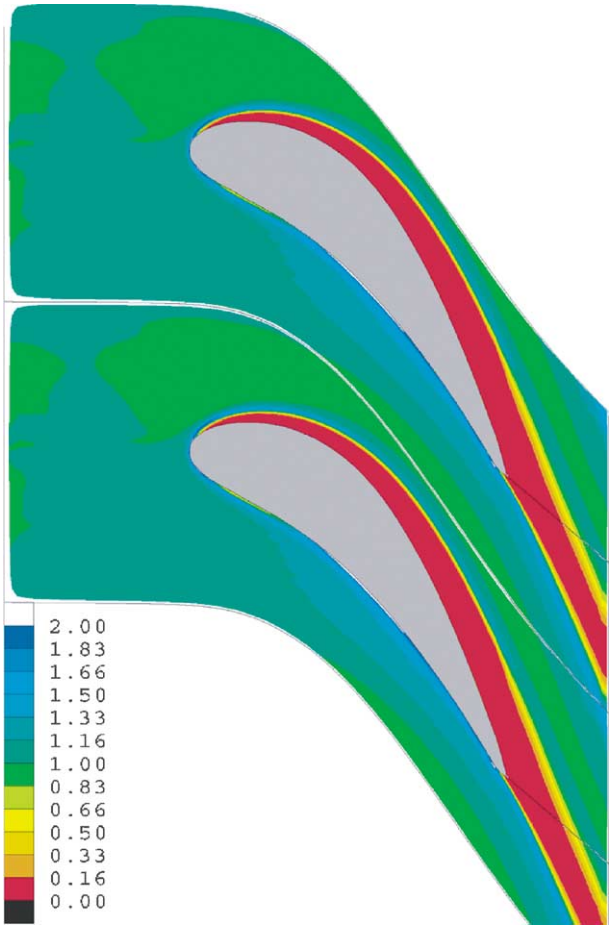

Fig. 13. Transport of 5 μm diameter particles in a turbine cascade. Contours of constant particle density (normalised by inlet value).

interpreting deposition distributions, it should be appreciated that τ_{p+} is not constant around the blade because of the strong variation of u_τ. Towards the rear of the pressure surface, which is the region of most interest, $\tau_{p+} \approx 1$ for the 5 μm particles under consideration.

Fig. 14a shows the deposition distribution when the only mechanisms included in the calculation are turbulent and Brownian diffusion. Only a tiny fraction ($F = 0.0008$) of the particles are deposited at the leading edge by Brownian diffusion and there is no deposition at all on the pressure surface. In Fig. 14b, inertial mechanisms are included in the calculation but both types of diffusion are excluded. F is now considerably higher with a value of 0.0205 (note the change in ordinate scale) with most particles depositing at the leading edge rather than on the pressure surface. The high deposition rate near the stagnation point is a result of the high streamline curvature in this region and is a well-known laminar effect. The lack of deposition on the pressure surface can be explained as follows. In the mainstream flow outside the boundary layer, streamline curvature causes a drift of particles towards the blade. When the particles enter the boundary

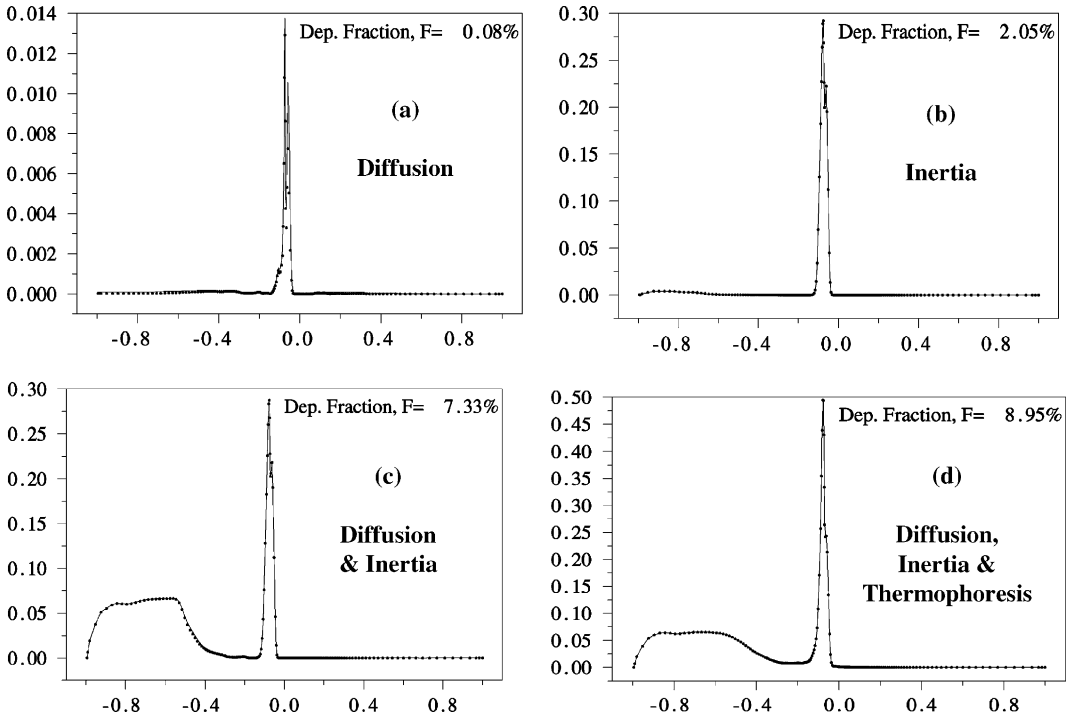

Fig. 14. Blade surface deposition distribution of 5 μm diameter particles in a turbine cascade plotted against normalised surface distance (suction surface positive, pressure surface negative). Note the different ordinate scales. (a) Diffusion only, no inertia, no thermophoresis, (b) inertia only, no diffusion, no thermophoresis, (c) inertia and diffusion, no thermophoresis, (d) inertia, diffusion and thermophoresis.

layer, they are decelerated and their pathlines bend towards the gas streamlines as described in Section 5. The deceleration for 5 μm particles, is such that they do not quite penetrate into the buffer layer ($y_+ < 40$) and hence are not influenced by turbophoresis. Apart from a very small region near the trailing edge, particles are not deposited and are instead transported out of the cascade within the boundary layer.

In Fig. 14c, both inertia and diffusion are included. The deposition at the leading edge is unchanged but that on the pressure surface is increased dramatically giving $F = 0.0733$. This is a graphic illustration of the fact that, when diffusion and inertia operate together, the total is not the sum of the parts considered in isolation. As before, streamline curvature causes a particle drift into the boundary layer. Inertia alone cannot maintain this flux to the wall but the addition of diffusion, aided by a favourable particle density gradient, allows the particles to reach the buffer layer, come under the influence of turbophoresis, and then deposit.

Finally, Fig. 14d shows the effect of including thermophoresis (once again, note the change in ordinate scale). Deposition on the pressure surface starts further upstream and F is increased by 22% from 0.0733 to 0.0895. This is a rather modest increase (compared with the changes due to thermophoresis shown in Fig. 7 for channel-flow with $\tau_{p+} \approx 1$) and is an indication of the importance of the centrifuging effect of streamline curvature which, in this case, tends to mask the contribution from thermophoresis.

7. Conclusions

The paper has addressed several aspects of particle deposition from turbulent gas flows using a fully-Eulerian calculation method for 2D flows. The main conclusions are:

(i) Density-weighted averaging combined with a simple particle turbulence model results in equations similar to those obtained by YL97 using non-density-weighted averaging. The fact that YL97 neglected a turbulence correlation involving particle compressibility points to a possible over-sight in conventional density-weighted turbulence modelling.
(ii) Improved particle turbulence modelling *might* result from introducing higher order equations into the analysis but this needs to be done without obscuring the physics by the mathematics. The status of the theory is such that more complex models should be introduced cautiously and only when well-substantiated, preferably by experimental data.
(iii) Decomposition of the particle flux into convective and diffusive components is useful both for exposing the different rôles of diffusion and turbophoresis and for developing the numerical solution technique. It is believed that the analysis presented here provides a clearer picture of the characteristics of turbulent gas–particle flows than other treatments.
(iv) Deposition from turbulent channel-flow was used to validate the modelling assumptions. The agreement with pipe-flow data is good, although a comparison with YL97 showed differences in the near-wall particle behaviour. The 2D calculations allow the developing region of a channel-flow to be investigated. This is of engineering interest and also useful for interpreting experimental data. The computer code was shown to have the capability of predicting deposition rates which vary by four or five orders of magnitude.
(v) The effect of thermophoresis in non-isothermal flows can have a dramatic effect on deposition rates for $\tau_{p+} < 10$. The calculations have been compared with some new experimental data and the agreement, although still tentative, is good.
(vi) Calculations of a boundary layer flow for two particle sizes have been presented. The smaller particles show how particle slip caused by streamline curvature can modify the deposition rates by interacting with the other transport mechanisms. Such interactions in a boundary layer require much more investigation.
(vii) Deposition in a turbine cascade has been used to illustrate the computational capability in more complex geometries. The calculations showed that pressure surface deposition resulted from an interplay between streamline curvature, particle inertia, turbophoresis and diffusion and cannot be predicted by considering each effect in isolation. For the chosen test condition, the inclusion of thermophoresis produced only a moderate increase in deposition rate due to the dominant effect of streamline curvature.

In summary, the paper has shown that simple particle turbulence modelling, combined with a physically-based approach to equation handling can give rise to a flexible calculation scheme for predicting deposition from complex 2D turbulent flows. Application of the method to three very different flow geometries has illustrated its potential and has highlighted a number of areas for future investigation, both in the physics of the turbulence modelling and in the interaction of the different phenomena responsible for particle transport.

Acknowledgements

The work was carried out at the Whittle and Hopkinson Laboratories, Cambridge University Engineering Department. SAS and ADL received EPSRC research studentships and maintenance contributions from the PowerGen, Power Technology Centre. ADL also received a grant from the W.G. Collins fund of the Cambridge Engineering Department and an External Research Studentship from Emmanuel College, Cambridge. The authors wish to thank Dr. J. Fackrell, Mr. K. Brown and Dr. D. Hobson of PowerGen for their support and technical advice.

Appendix A. Gas–particle turbulence correlations

Consider first the density-weighted correlation of Eq. (9a), $\overline{\overline{(u_i'v_j'')}}$. Various methods have been used to model this term, all giving essentially the same result. The following approach, based on a fixed point integration, helps to identify the assumptions. Neglecting all forces except viscous drag, Eqs. (1a) and (1b) are first combined to give,

$$\frac{\partial v_j}{\partial t} + v_k \frac{\partial v_j}{\partial x_k} = \frac{u_j - v_j}{\tau_p} \tag{A.1a}$$

Eq. (5) for the j-direction is,

$$\frac{\partial \overline{\overline{V_j}}}{\partial t} + \overline{\overline{V_k}} \frac{\partial \overline{\overline{V_j}}}{\partial x_k} = \frac{\overline{U}_j - \overline{\overline{V_j}}}{\tau_p} + \frac{1}{\bar{\rho}_p}\left[\frac{\bar{\rho}_p \overline{\overline{u_j'}}}{\tau_p} - \frac{\partial \bar{\rho}_p \overline{\overline{(v_j'' v_k'')}}}{\partial x_k}\right] \tag{A.1b}$$

Subtraction then gives a differential equation for the particle fluctuating velocity,

$$\frac{\partial v_j''}{\partial t} + \frac{v_j''}{\tau_p} = \frac{u_j'}{\tau_p} - v_k \frac{\partial v_j}{\partial x_k} - \frac{1}{\bar{\rho}_p}\left\{\frac{\bar{\rho}_p \overline{\overline{u_j'}}}{\tau_p} - \frac{\partial \bar{\rho}_p \overline{\overline{(v_j'' v_k'')}}}{\partial x_k} - \bar{\rho}_p \overline{\overline{V_k}} \frac{\partial \overline{\overline{V_j}}}{\partial x_k}\right\} \tag{A.2}$$

The term in braces involves only ensemble-mean quantities and will be denoted EM. Integrating from $-\infty$ to t at constant x_i gives,

$$v_j''(t) = \frac{e^{-t/\tau_p}}{\tau_p} \int_{-\infty}^{t} e^{z/\tau_p}\left(u_j'(z) - \tau_p v_k(z) \frac{\partial v_j(z)}{\partial x_k} - \tau_p \mathrm{EM}\right) dz \tag{A.3}$$

Eq. (A.3) is multiplied through by $\rho_p(t)u_i'(t)$ [the $\rho_p(t)$ is important and is not normally included] and the dummy variable z is changed to $s = t - z$. Ensemble averaging then gives,

$$\overline{\overline{u_i' v_j''}} = \frac{1}{\tau_p} \int_0^{\infty} e^{-s/\tau_p} \overline{\overline{[u_i'(0)u_j'(s)]}}\, ds - \int_0^{\infty} e^{-s/\tau_p} \overline{\overline{\left[u_i'(0) v_k(s) \frac{\partial v_j(s)}{\partial x_k}\right]}}\, ds - \tau_p \mathrm{EM} \overline{\overline{u_i'}} \tag{A.4}$$

This expression is valid for inhomogeneous turbulent flows but in order to make progress it is necessary to drop the second and third terms on the RHS. The Eulerian autocorrelation function for the carrier gas is then defined in the usual way by (no summation),

$$R_{ij}(s) = \frac{\overline{u_i'(0)u_j'(s)}}{\overline{u_i'(0)u_j'(0)}} \tag{A.5}$$

Substituting into Eq. (A.4), *ignoring the requirement for a density-weighted correlation*,

$$\overline{\overline{u_i'v_j''}} \cong \overline{u_i'u_j'}\frac{1}{\tau_p}\int_0^\infty e^{-s/\tau_p}R_{ij}(s)\,ds \tag{A.6}$$

If R_{ij} is assumed to be isotropic, then $R_{ij}(s) = \delta_{ik}R(s)$. This gives Eqs. (9) in the main text,

$$\overline{\overline{u_i'v_j''}} \cong \Gamma\overline{(u_i'u_j')} \tag{A.7}$$

$$\Gamma = \frac{1}{\tau_p}\int_0^\infty e^{-s/\tau_p}R(s)\,ds \tag{A.8}$$

The integral time-scale τ_g is defined by,

$$\tau_g = \int_0^\infty R(s)\,ds \tag{A.9}$$

Consider now the density-weighted correlation $\overline{\overline{u_i'}}$. Subtracting Eq. (3a) from (1a) gives (for a stationary flow with $\partial\bar{\rho}_p/\partial t = 0$),

$$\frac{\partial\rho_p}{\partial t} = -v_k''\frac{\partial\bar{\rho}_p}{\partial x_k} - \bar{\rho}_p\frac{\partial v_k''}{\partial x_k} - \frac{\partial\rho_p'v_k}{\partial x_k} \tag{A.10}$$

Neglecting the second and third terms on the RHS (without any real justification, it must be said) and integrating at constant x_i from $-\infty$ to t gives,

$$\rho_p(t) \cong \rho_p(-\infty) - \frac{\partial\bar{\rho}_p}{\partial x_k}\int_{-\infty}^t v_k''(\eta)\,d\eta \tag{A.11}$$

From Eq. (A.3), neglecting the second and third terms in the brackets,

$$v_k''(\eta) = \frac{e^{-\eta/\tau_p}}{\tau_p}\int_{-\infty}^\eta e^{z/\tau_p}u_k'(z)\,dz \tag{A.12}$$

Substituting Eq. (A.12) into (A.11) and integrating by parts gives,

$$\rho_p(t) \cong \rho_p(-\infty) - \frac{\partial\bar{\rho}_p}{\partial x_k}\int_{-\infty}^t u_k'(z)(1 - e^{-(t-z)/\tau_p})\,dz \tag{A.13}$$

Eq. (A.13) is now multiplied through by $u_i'(t)$ and the dummy integration variable changed to $s = t - z$. After ensemble averaging and introducing Eq. (A.5),

$$\overline{\rho_p u_i'} = \bar{\rho}_p\overline{\overline{u_i'}} \cong -\frac{\partial\bar{\rho}_p}{\partial x_k}\overline{(u_i'u_k')}\int_0^\infty (1 - e^{-s/\tau_p})R_{ik}(s)\,ds \tag{A.14}$$

Writing $R_{ij}(s) = \delta_{ik}R(s)$ as before and noting Eqs. (A.8) and (A.9), gives,

$$\bar{\rho}_p\overline{\overline{u_i'}} \cong -(\tau_g - \tau_p\Gamma)\overline{(u_i'u_k')}\frac{\partial\bar{\rho}_p}{\partial x_k} \tag{A.15}$$

Introducing Γ from Eq. (10) then gives Eq. (12a).

References

Beal, S.K., 1970. Deposition of particles in turbulent flow on channel or pipe walls. Nucl. Sci. Engng. 40, 1–11.

Caporaloni, M., Tampieri, F., Trombetti, F., Vittori, O., 1975. Transport of particles in nonisotropic air turbulence. J. Atmos. Sci. 32, 565–568.

Cerbelli, S., Giusti, A., Soldati, A., 2001. ADE approach to predicting dispersion of heavy particles in wall-bounded turbulence. Int. J. Multiphase Flow 27, 1861–1879.

Derevich, I.V., 1999. Statistical model for particles turbulent deposition in a pipe flow. In: Celata, G.P., Di Marco, P., Shah, R.K. (Eds.), Two-Phase Flow Modelling and Experimentation, pp. 1161–1170.

Derevich, I.V., Zaichik, L.I., 1988. Particle deposition from turbulent flow. Fluid Dyn. 23, 722–729.

Gosman, A.D., Ioannides, E., 1983. Aspects of computer simulation of liquid fuelled combustors. J. Energy 7, 482–490.

Healy, D.P., Young, J.B., 2001. Calculation of inertial particle transport using the Osiptsov Lagrangian method. 4th Int. Conf. on Multiphase Flow, New Orleans, Paper DJ4.

Hirsch, C., 1990. In: Numerical Computation of Internal and External Flows, vol. 1. Wiley-Interscience, pp. 253–255.

Hyland, K.E., Reeks, M.W., 1997. Constitutive relations for dispersed particles in nonuniform flows. ASME Fluids Eng. Div. Summer Meeting, FEDSM'97, Paper 3686.

Kallio, G.A., Reeks, M.W., 1989. A numerical simulation of particle deposition in turbulent boundary layers. Int. J. Multiphase Flow 15, 433–446.

Leeming, A.D., 1995. Particle Deposition from Turbulent Flows. Ph.D. thesis, Cambridge University Engineering Department.

Liu, B.Y., Agarwal, J.K., 1974. Experimental observation of aerosol deposition in turbulent flow. J. Aerosol Sci. 5, 145–155.

Morsi, S.A., Alexander, A.J., 1972. An investigation of particle trajectories in two-phase flow systems. J. Fluid Mech. 55, 193–208.

Pismen, L.M., Nir, A., 1978. On the motion of suspended particles in an isotropic turbulent fluid. J. Fluid Mech. 84, 193–206.

Rambaud, P., Oesterlé, B., Tanière, A., 2002. Assessment of integral time scales in a gas–solid channel flow with relevance to particle dispersion modelling. In: Sommerfeld, M. (Ed.), Proc. 10th Workshop on Two-Phase Flow Predictions, Merseburg, pp. 182–194.

Ramshaw, J.D., 1979. Brownian motion in a flowing fluid. Phys. Fluids 22, 1595–1601.

Reeks, M.W., 1977. On the dispersion of small particles suspended in an isotropic turbulent fluid. J. Fluid Mech. 83, 529–546.

Reeks, M.W., 1983. The transport of discrete particles in inhomogeneous turbulence. J. Aerosol Sci. 14, 729–739.

Reeks, M.W., 1991. On a kinetic equation for the transport of particles in turbulent flows. Phys. Fluids A 3, 446–456.

Reeks, M.W., 1992. On the continuum equations for dispersed particles in nonuniform flows. Phys. Fluids A 4, 1290–1303.

Saffman, P.G., 1965. The lift on a small sphere in a slow shear flow. J. Fluid Mech. 22, 385–400, Corrigendum, 1968, 32, 624.

Simonin, O., Viollet, P.L., 1990. Modelling of turbulent two-phase jets loaded with discrete particles. In: Int. Sem. on Interface Phenomena in Multiphase Flows, Dubrovnik, pp. 259–269.

Simonin, O., Deutsch, E., Minier, M., 1993. Eulerian prediction of the fluid/particle correlated motion in turbulent two-phase flows. Appl. Sci. Res. 51, 275–283.

Simonin, O., Wang, Q., Squires, K.D., 1997. Comparison between two-fluid model predictions and large eddy simulation results in a vertical gas–solid turbulent channel flow. ASME, Fluids Eng. Div. Summer Meeting, FEDSM'97, Paper 3625.

Slater, S.A., Young, J.B., 2001. The calculation of inertial particle transport in dilute gas-particle flows. Int. J. Multiphase Flow 27, 61–87.

Squires, K.D., Eaton, J.K., 1991. Measurements of particle dispersion obtained from direct numerical simulations of isotropic turbulence. J. Fluid Mech. 226, 1–35.

Talbot, L., Cheng, R.K., Schefer, R.W., Willis, D.R., 1980. Thermophoresis of particles in a heated boundary layer. J. Fluid Mech. 101, 737–758.

Tsirkunov, Yu.M., 2001. Gas-particle flows around bodies—key problems, modelling and numerical analysis. 4th Int. Conf. Multiphase Flow, ICMF-2001, New Orleans.

Wang, Q., Squires, K.D., Chen, M., McLaughlin, J.B., 1997. On the role of the lift force in turbulence simulations of particle deposition. Int. J. Multiphase Flow 23, 749–763.

Wang, Q., Squires, K.D., Simonin, O., 1998. Large eddy simulation of turbulent gas–solid flows in a vertical channel and evaluation of second-order models. Int. J. Heat Fluid Flow 19, 505–511.

Young, J.B., Leeming, A.D., 1997. A theory of particle deposition in turbulent pipe flow. J. Fluid Mech. 340, 129–159.